

RESEARCH ARTICLE

10.1002/2013JA019595

Key Points:

- EMIC waves are modeled using RAM-SCM-HOTRAY for GEM challenge events
- Simulations agree with in situ EMIC events at five geosynchronous satellites
- EMIC wave simulation agrees with proton aurora images from IMAGE satellites too

Correspondence to:

L. Chen,
lunjin.chen@gmail.com

Citation:

Chen, L., V. K. Jordanova, M. Spasojević, R. M. Thorne, and R. B. Horne (2014), Electromagnetic ion cyclotron wave modeling during the geospace environment modeling challenge event, *J. Geophys. Res. Space Physics*, 119, doi:10.1002/2013JA019595.

Received 4 NOV 2013

Accepted 24 MAR 2014

Accepted article online 27 MAR 2014

Electromagnetic ion cyclotron wave modeling during the geospace environment modeling challenge event

Lunjin Chen¹, Vania K. Jordanova², Maria Spasojević³, Richard M. Thorne⁴, and Richard B. Horne⁵
¹Department of Physics, University of Texas at Dallas, Richardson, Texas, USA, ²Los Alamos National Laboratory, Los Alamos, New Mexico, USA, ³Space, Telecommunications and Radio Science Laboratory, Stanford University, Stanford, California, USA, ⁴Department of Atmospheric and Oceanic Sciences, University of California, Los Angeles, Los Angeles, California, USA, ⁵British Antarctic Survey, Natural Environment Research Council, Cambridge, UK

Abstract We investigate the temporal evolution and the spatial distribution of electromagnetic ion cyclotron (EMIC) waves during the 8–11 June 2001 geomagnetic storm, one of the storms selected for study by the Geospace Environment Modeling program. Generations of EMIC waves in the H⁺, He⁺, and O⁺ bands are simulated using the kinetic ring current-atmosphere interactions model with a self-consistent magnetic field and a ray tracing code. Simulations show that strong wave gain occurs in the afternoon sector at $L > 5$ and overlaps with a high-density plasmaspheric drainage plume. EMIC wave gain maximizes during the main phase and decreases in the recovery phase. We find that EMIC wave gain is stronger in the He⁺ band than in the other two bands in the inner magnetosphere, except the region of low L (< 3) where the H⁺ band is dominant due to an enhancement in the ring current anisotropy. Little wave gain is obtained for the O⁺ band. Comparison with in situ EMIC events and EMIC event proxies at five geosynchronous satellites shows consistence in the temporal and local time evolution of the wave distribution. Our simulations of the EMIC wave distribution also agree with proton aurora at subauroral latitudes observed from the Imager for Magnetopause-to-Aurora Global Exploration satellite.

1. Introduction

Electromagnetic ion cyclotron (EMIC) waves play important roles as intermediaries in the interplay between various plasma populations in the magnetosphere, including the plasmasphere, ring current, and radiation belts (see a review by Thorne *et al.* [2006]). EMIC waves are naturally occurring emission that are generated by the temperature anisotropy of the energetic ring current ions [Jordanova *et al.*, 2001, 2006; Chen *et al.*, 2010], preferentially near the equatorial region [Loto'aniu *et al.*, 2005] and on the duskside during storm time conditions [Erlandson and Ukhorskiy, 2001; Fraser *et al.*, 2010]. The generation and propagation characteristics of the waves are affected by the low-energy thermal plasmas, including thermal electron number density [Chen *et al.*, 2009] and composition of heavier ions than H⁺ [Gomberoff and Neira, 1983; Young *et al.*, 1981; Kozyra *et al.*, 1984]. Fine-scale density structures with the thermal plasma inside a plasmaspheric plume also enhance wave amplification further due to the guidance of waves by the density gradients [Chen *et al.*, 2009; Soria-Santacruz *et al.*, 2013]. The generated EMIC waves can produce pitch angle scattering of ring current protons, leading to proton precipitation [Xiao *et al.*, 2011; Sakaguchi *et al.*, 2012] and thus the formation of proton aurora at subauroral latitudes [Cornwall *et al.*, 1970, 1971; Spasojević *et al.*, 2004; Yahnin and Yahnina, 2007; Spasojević *et al.*, 2011; Yahnin *et al.*, 2013]. EMIC waves can also heat thermal electrons via Landau resonant interaction [Thorne *et al.*, 2006] and produce pitch angle scattering of much more energetic ($> \text{MeV}$) radiation belt electrons via cyclotron resonant interaction. The latter has been proposed [e.g., Thorne and Kennel, 1971] to account for relativistic electron dropout during the main phase of geomagnetic storms. The precipitation of ring current protons and radiation belt electrons induced by EMIC waves was demonstrated in simulations [e.g., Jordanova *et al.*, 2008] and has been confirmed with multiple conjugate measurements [e.g., Miyoshi *et al.*, 2008].

Various numerical methods have been used to understand the generation of EMIC waves, including but not limited to linear theory [e.g., Gary *et al.*, 2012; Chen *et al.*, 2011], hybrid particle simulations [e.g., Hu *et al.*, 2010; Shoji *et al.*, 2011; Omid *et al.*, 2013], and global ring current modeling [e.g., Jordanova *et al.*, 2001, 2006; Chen *et al.*, 2010]. Besides cyclotron instabilities due to ion temperature anisotropy, mode conversion of compressional waves at the ion-ion hybrid resonance [Lee *et al.*, 2008] has also been proposed as a

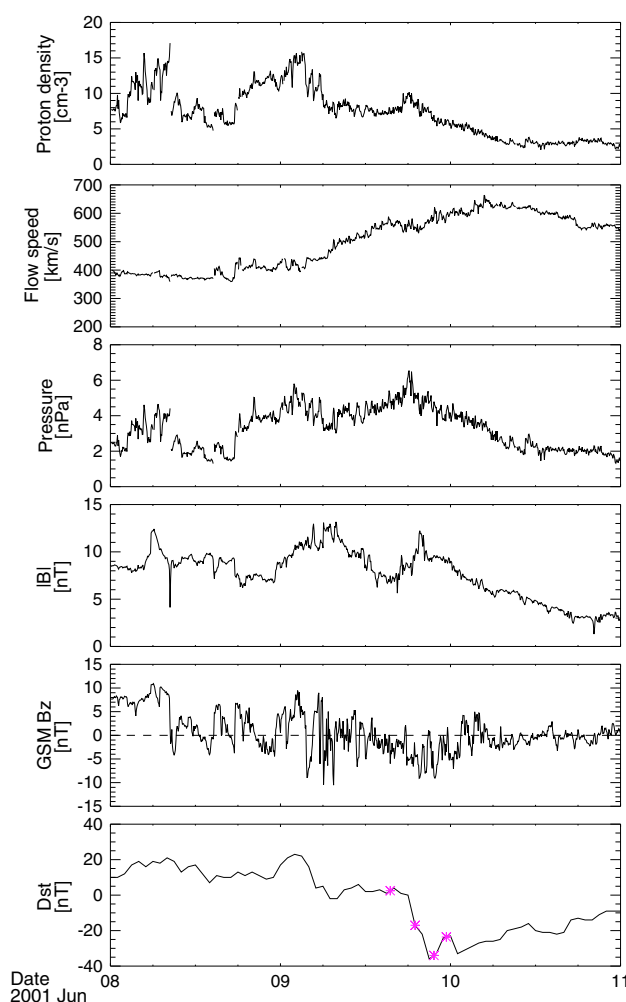


Figure 1. Interplanetary solar wind data from OMNI (with time shifted to the magnetopause) during 8–11 June 2001 geomagnetic storm. (a) Proton density, (b) solar wind speed, (c) solar wind pressure, (d) magnetic field strength, (e) B_z (GSM) component of the magnetic field, and (f) Dst index. Four magenta points mark times of interest on 9 June 15:30 (prestorm), 19:00 (main phase), 21:40 (Dst minimum), and 23:25 (recovery phase).

of this geomagnetic storm, we also compare the modeling results of EMIC waves against the EMIC wave observations and wave proxies from geosynchronous orbiting satellites and against proton aurora images taken from the Imager for Magnetopause-to-Aurora Global Exploration (IMAGE) satellite. The outline of this manuscript is organized as follows. The RAM-SCB and HOTRAY models are described in section 2, and modeling results for the ring current ions and EMIC waves are presented in section 3. EMIC wave model results are compared against the available observations in section 4, followed by conclusions and discussion on the future improvement of our model in section 5.

2. RAM-SCB and HOTRAY Model Description

To model the global characteristics of EMIC waves, the RAM-SCB model and the HOTRAY code [Horne, 1989] are used, where the former simulates the dynamics of ring current which stores free energy for EMIC waves and the latter simulates the propagation and excitation of EMIC waves. The RAM-SCB model itself couples two codes: (1) the ring current-atmosphere interactions model (RAM), which solves the bounce-averaged kinetic equation for the major ring current species [Jordanova et al., 1997, 2006, 2012] and (2) a 3-D Euler-potential-based plasma equilibrium code solving for the magnetic field [Zaharia et al., 2004, 2006; Zaharia, 2008; Zaharia et al., 2010]. RAM-SCB code assumes an equilibrium state where magnetic force is in balance with the plasma pressure gradient force. The resulting force-balanced magnetic field is

potential excitation mechanism for EMIC waves. To understand the global distribution of EMIC waves due to ring current ions, we use a coupled model, the kinetic ring current-atmosphere interactions model with self-consistent magnetic field (RAM-SCB) and a ray tracing code (HOTRAY), to investigate the evolution of ring current ions and EMIC waves for the 8–11 June 2001 geomagnetic storm. This event is one of geomagnetic storms selected by the Plasmasphere-Magnetosphere Interactions (PMI) focus group of the National Science Foundation's (NSF) Geospace Environment Modeling (GEM) program. The goal of the GEM/PMI modeling challenge is to evaluate the current state of space physics modeling capability as it relates to how the evolving global distribution of cold plasma governs the growth and propagation of EMIC waves and how wave-particle interactions affect the energetic particle distribution and dynamics. The solar wind parameters from ACE spacecraft and geomagnetic Dst index for this event are shown in Figure 1. The storm was caused by southward interplanetary magnetic field component, B_z , excursion down to -9 nT, and solar wind flow speed up to 650 km/s and produced a moderate level of Dst depression (~ -40 nT).

In addition to our modeling effort

calculated based on the plasma pressure produced by the ring current particles and in turn affects the motions of ring current particles and thus their phase space distribution function. The 4-D kinetic RAM evaluates numerically the bounce-averaged distribution function for H^+ , O^+ , and He^+ ions in the magnetic equatorial plane as a function of radial distance from Earth (R_o from 2 to $6.5 R_E$), magnetic local time (MLT), kinetic energy from 100 eV to 400 keV, and equatorial pitch angle from 0° to 90° .

The RAM model calculates the adiabatic transport of ring current ions by evaluation of bounce-averaged electric and magnetic drift velocity, based on the conservation of the first and second adiabatic invariants and using a time-dependent electric and magnetic field model (updated at 5 min time intervals). The magnetic field is calculated through the SCB code using a computational 3-D equilibrium approach in flux coordinates (Euler potentials) (for more details, see *Zaharia et al.* [2004] and *Zaharia* [2008]) and solving the single-fluid plasma force-balance equation, where the plasma pressure gradient force of ring current ions is provided by the RAM [e.g., *Jordanova et al.*, 2012]. The inner and outer magnetic flux surface of SCB is obtained by the field line tracing using the empirical *Tsyganenko and Sitnov* [2005] magnetic field model. The empirical convection electric field model of *Weimer* [2001] (W01), in addition to the time-independent corotation electric field model, is implemented. The W01 ionospheric potential is driven by time-dependent interplanetary data and the AL index and is mapped to the solar magnetic (SM) equatorial plane along the SCB field lines. The RAM model also includes loss processes for ring current ions, including charge exchange with geocoronal hydrogen, Coulomb collisions with thermal plasma, and loss due to collisions with the dense atmosphere at low altitudes (for more details, see *Jordanova et al.* [1996, 2001]). We note that wave-particle interactions are not included in this model so there is no plasma wave scattering feedback on the particle distributions. The RAM model is coupled with the time-dependent plasmasphere model of *Rasmussen et al.* [1993], where the thermal electron density in the equatorial plane is calculated by following the $E \times B$ drift motion of individual flux tubes and ionospheric supply and loss are also considered. To set the initial conditions for the RAM model, we use quiet time data from the HYDRA and MICS instruments on the Polar satellite and run the model for more than 10 h of quiet time before storm commencement. The nightside boundary conditions for the ring current ions are determined from plasma sheet flux measurements from the Magnetospheric Plasma Analyzer and Synchronous Orbit Particle Analyzers instruments on the LANL geosynchronous spacecraft. The MLT dependence of the data for the nightside boundary is preserved, and the dependence of the ion composition with geomagnetic and solar activity is adopted using the *Young et al.* [1982] study. The dayside boundary conditions correspond to free particle outflow.

The phase space density (PSD) of energetic ring current ions and the plasmaspheric electron density obtained from the RAM simulation are used as input to the HOTRAY code to evaluate the path-integrated gain of EMIC waves. The HOTRAY code [*Horne*, 1989] has been extensively applied to studies of electromagnetic and electrostatic waves, including EMIC waves in the Earth's magnetosphere [e.g., *Horne and Thorne*, 1993, 1994]. The code can trace any type of wave in a hot magnetized plasma with weak growth or damping, provided the wave growth remains linear. The ray tracing method assumes that gradients in the medium, notably the plasma density and magnetic field gradients, are small compared to the wavelength and that the gradients remain continuous. The mode conversion [e.g., *Johnson and Cheng*, 1999], which likely occurs when dispersion solutions of different modes are sufficiently close, can not also be treated by the ray tracing. The ray tracing equations [*Horne*, 1989, equations (1) and (2)] are integrated with respect to time to find the new position and wave number at each time step. We use faster and more reliable cold plasma ray tracing, to save computation time and avoid various issues regarding ray tracing in hot plasma, and to obtain raypath-integrated wave gain, we instead implement the growth rate solver, which yields linear growth rate for an arbitrary phase space density distribution [e.g., *Chen et al.*, 2010].

The ray tracing requires the 3-D configuration of magnetic field and cold plasma. Currently, a dipolar magnetic field, instead of the magnetic field from SCB model, is implemented in the HOTRAY code. The 3-D cold plasma density model is set up based on the plasma density on the equatorial plane from the *Rasmussen et al.* [1993] plasmaspheric model and the assumption of constant density along a field line. This assumption is not critical since the source of EMIC wave excitation is confined to within about 10° latitude of the equator. The subsequent propagation and reflection at high latitude [e.g., *Thorne and Horne*, 1992, 1994; *Horne and Thorne*, 1997] would not provide significant wave amplification due to wave refraction. Since the fractional thermal ion composition greatly affects propagation characteristics of EMIC waves and is not explicitly simulated in the Rasmussen model, a typical storm time thermal ion composition, $\eta_{H^+} = 77\%$, $\eta_{He^+} = 20\%$, and $\eta_{O^+} = 3\%$, is assumed, following *Jordanova et al.* [2008]. A ray with a specific frequency (f) is launched

at the equator along the magnetic field line at a specific L shell and magnetic local time and traced by the ray tracing code, which provides the time evolution of the ray trajectory and the wave normal direction. The growth rate solver [Chen *et al.*, 2010, equation (2)] evaluates the growth/damping rate along the ray trajectory, based on velocity distribution of energetic H^+ ions. The contribution of resonance harmonics m from -5 to 5 is included in the growth rate calculation. Ring current H^+ ions are used for the growth rate evaluation. The H^+ ion velocity distribution for the growth rate solver assumes bi-Maxwellian distribution with number density, parallel temperature, and perpendicular temperature obtained by the evaluation of first and second moments of simulated velocity distribution (at any spatial location) from the RAM model. The wave path-integrated gain, representing the amplification from the background noise level, is obtained via [e.g., Chen *et al.*, 2010]

$$\text{Gain, dB} = 20 \log_{10}(\exp(\int \gamma dt)),$$

where γ is wave temporal growth rate and t is time of propagation. It should be noted that the path-integrated gain of waves launched at the equator only represents one half of the net wave gain in the system, since we only consider propagation on one side of the equator. An identical wave gain can be obtained if the wave is traced backward in time and towards the southern hemisphere.

3. Results

3.1. RAM-SCB Results

Based on the availability of observational data for comparison, we select four times from 9 June 2001 to present our simulation results at different phases of the storm: specifically $t_1 = 15:30$ (prestorm), $t_2 = 19:00$ (main phase), $t_3 = 21:40$ (Dst minimum), and $t_4 = 23:25$ (early recovery phase), which are marked as magenta asterisks in Figure 1. Note that there is another small dip in Dst at 06:00 on the same day, indicating there may have some geomagnetic activities before t_1 .

Figure 2 shows simulated equatorial distribution cold plasma density on the top row. The magenta lines delineate the 50 cm^{-3} contour of the cold plasma density, which approximates, but do not exactly represent, the local time-dependent plasmopause location. While negative interplanetary B_z persists, the convection electric field is enhanced from t_1 to t_3 . As a consequence, a high-density plasmaspheric drainage plume forms in the local time sector from afternoon to dusk, and the plasmasphere shrinks at other local times. At t_4 during the recovery phase, the reduction of the convection electric field leads to wrapping of the plasmaspheric plume due to differential eastward angular drifting speed and the formation of a positive radial density gradient in the early afternoon sector [Spasojević *et al.*, 2003].

Ring current H^+ total pressure, parallel temperature, and temperature anisotropy at the four selected time intervals are shown in the bottom three rows of Figure 2. The calculation of these quantities is based on evaluation of the zero-order and the second-order velocity moments of the simulated ring current H^+ phase space density. The injection of plasma sheet ions during the main phase leads to an enhancement of partial ring current ion pressure in the localized local time sector between dusk and premidnight. During the recovery phase, the ring current ions drift westward, becoming more symmetric in local time (at t_4), and the pressure becomes weaker due to effect of loss processes. There are two preferential regions of enhanced ring current temperature anisotropy A , where A is defined $T_{\perp}/T_{\parallel} - 1$ and T_{\perp}/T_{\parallel} is the ratio of perpendicular to parallel temperature. A is as high as 2 in the inner L shells ($L < \sim 4$) at all local times, and $A \sim 1$ in the dusk sector at $L > \sim 5$ (the last row of Figure 2). The reason for high ring current ion anisotropy in the low L region is primarily due to preferential acceleration in the perpendicular direction over in the parallel direction as ions convect earthward, where the perpendicular energy scales as $1/L^3$ due to the conservation of the first adiabatic invariant while the parallel energy scales as $1/L^{5/2}$ due to the conservation of the second adiabatic invariant [e.g., Trakhtengerts and Rycroft, 2008]. Pitch angle-dependent losses, where particles with lower pitch angles and thus lower mirroring altitudes are subject to higher charge-exchange losses, are also important for $L < \sim 4$. In the high L region, the high anisotropy is a result of pitch angle-dependent magnetic gradient and curvature drift speeds and drift shell splitting (for further discussion see Jordanova *et al.* [2010]). The temperature of the low L region is less than the temperature of the high L region (the third row of Figure 2) due to the fact that ions of lower energy can penetrate more earthward while the more energetic ions tend to be prevented from drifting earthward due to greater azimuthal magnetic drift velocities.

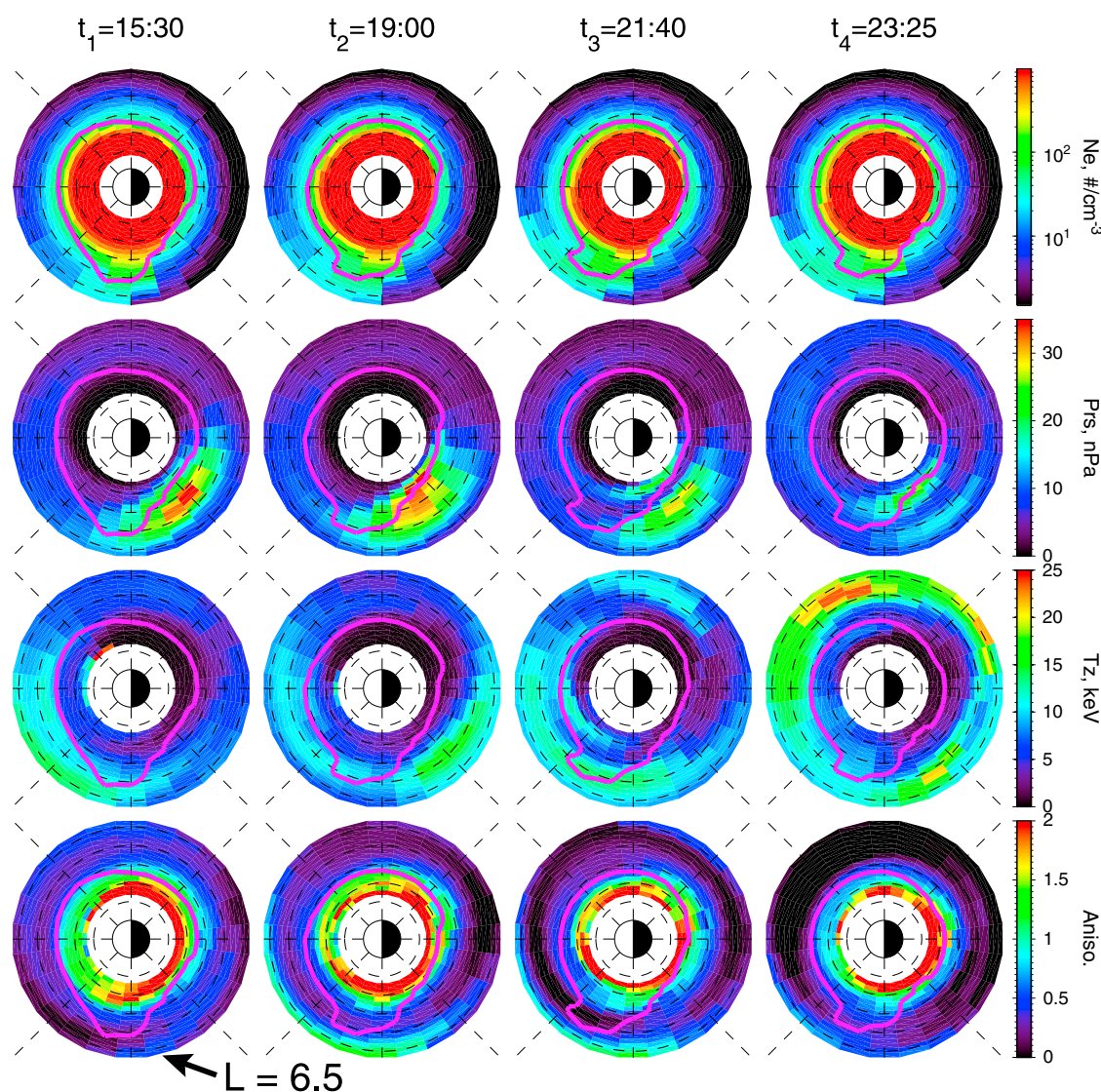


Figure 2. From top to bottom, cold plasma density, ring current pressure, ring current parallel temperature, and anisotropy from the RAM-SCB simulation as a function of radial distance in the equatorial plane and MLT at the four selected times on 9 June 2001 (represented by columns). Magenta lines delineate the contour of cold plasma density of 50 cm^{-3} .

3.2. HOTRAY Results

We use both cold plasma and ring current ion output from RAM-SCB to set up the plasma environment for the HOTRAY code. The cold plasma output is used to set up the magnetospheric medium in which ray tracing of EMIC waves is performed, while the ring current ion output is used to calculate the growth rate of EMIC waves. The combination of EMIC wave instability and propagation yields the path-integrated wave gain. The path-integrated wave gain does not yield the wave real amplitude but does indicate the level of amplification from the background noise level.

The ray tracing results for $L = 6$ and MLT = 17 at $t = t_2$ (main phase) are shown in Figure 3, which serves as an example to summarize the propagation characteristics of cold plasma waves below the proton gyrofrequency f_{H+} . The dispersion relation of the two cold plasma wave modes is plotted in Figure 3a at three different wave normal angles $\theta = 0^\circ$ (blue), 45° (green), and 90° (red), with y axis being normalized wave frequency, f/f_{H+} , and x axis the refractive index n . A variety of characteristic frequencies appear in addition to fundamental heavy ion cyclotron frequencies f_{He+} and f_{O+} , for He^+ and O^+ ions, respectively. These characteristic frequencies, which are defined in detail in Appendix 1, include two crossover frequencies f_{cr1} and f_{cr2} , two cutoff frequencies f_{cut1} and f_{cut2} , and two bi-ion frequencies f_{bi1} and f_{bi2} , where subscripts 1 and 2 denote

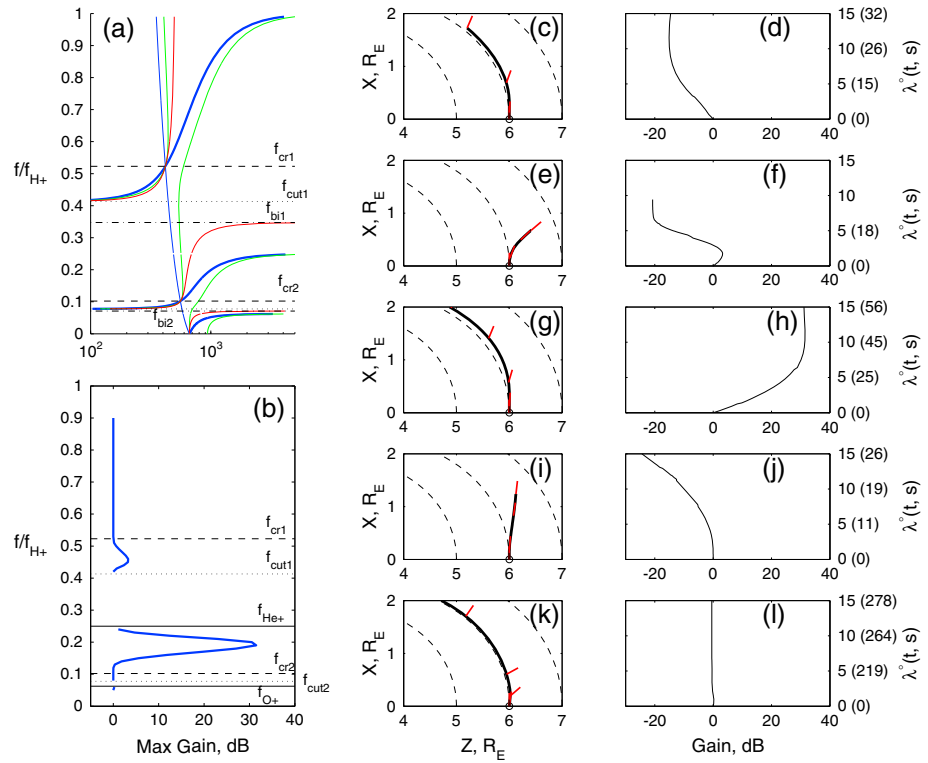


Figure 3. Ray tracing examples at $L = 6$, MLT = 17 at 19:00 9 June 2001. (a) Dispersion relation between wave frequency and wave refractive index for wave normal angle 0° (blue), 45° (green), and 90° (red). Parallel propagating left-handed mode is marked as thick blue lines. (b) The maximum path-integrated gain versus wave frequency. Also shown are raypaths (black solid lines in the middle column) and path-integrated gain versus latitude (black solid lines in the last column) for examples of wave frequencies, (c, d) $0.6 f_{H+}$, (e, f) $0.45 f_{H+}$, (g, h) $0.19 f_{H+}$, (i, j) $0.1 f_{H+}$, and (k, l) $0.06 f_{H+}$. In the middle column, black dashed lines denotes the field lines of $L = 4, 5$, and 6 , and red line segments denote the direction of wave normals along raypaths. In the last column, the numbers in the parentheses are the corresponding times in second when rays pass through a specific latitude.

the frequency in the range $[f_{He+}, f_{H+})$ and $[f_{O+}, f_{He+})$, respectively. For the cold ion composition specified in this study (77% H^+ , 20% He^+ , and 3% O^+), the corresponding characteristic frequencies can be evaluated and shown as horizontal lines in Figure 3a, being sorted by value in descending order, $f_{cr1} = 0.52 f_{H+}$, $f_{cut1} = 0.41 f_{H+}$, $f_{bi1} = 0.35 f_{H+}$, $f_{cr2} = 0.102 f_{H+}$, $f_{cut2} = 0.078 f_{H+}$, and $f_{bi2} = 0.071 f_{H+}$.

Since the ring current H^+ temperature anisotropy provides the free energy to drive unstable left-handed waves and the strongest growth rate generally occurs for parallel propagation, ray tracing is only performed for the left-handed parallel propagating modes. The right-handed mode with parallel propagating mode is always stable or damped by the ring current ions and will not be traced. The selected wave modes for launch are marked as three thick blue lines in Figure 3a, which represent the three wave frequency bands, the H^+ band ($f_{cut1} < f < f_{H+}$), the He^+ band ($f_{cut2} < f < f_{He+}$), and the O^+ band ($0 < f < f_{O+}$). For the H^+ band or the He^+ band, one may further divide the frequency band into two bands, one above and the other one below the corresponding crossover frequency as a result of different propagation characteristics. For example, raypaths for $f = 0.6 f_{H+}$ ($f_{cr1} < f < f_{H+}$) and $f = 0.45 f_{H+}$ ($f_{cut1} < f < f_{cr1}$), shown in Figures 3c and 3e respectively, show distinct features. The ray above the crossover frequency propagates almost along the same field line while the ray below the crossover frequency quickly deviates the field line at launch and propagate toward larger L . The difference lies in the fact that the two rays belong to the two different kinds of dispersion surfaces [Rauch and Roux, 1982]. The left-handed mode in the H^+ band with $f_{cr1} < f < f_{H+}$ has group velocity direction almost parallel to the magnetic field line, with little dependence on the wave normal angle. The feature can be seen in Figure 3c, where wave normal direction (red short segments) becomes more and more oblique during propagation but raypath remains along the field line. In contrast, the left-handed mode in the H^+ band with $f_{cut1} < f < f_{cr1}$ has group velocity direction almost parallel to the direction of wave normal. This can be seen in Figure 3e showing that the wave normal vectors

(red short segments) are parallel to the ray trajectory. Nonetheless, the two frequency bands in the H^+ band share a common feature, i.e., the wave normal direction becomes more oblique as waves propagate away from the equator because of the wave refraction caused by the magnetic gradient and curvature in the dipole field. Similarly, the He^+ band can be further divided into two subranges, $f_{cr2} < f < f_{He+}$ for which the group velocity is almost along the magnetic field line and $f_{cut2} < f < f_{cr2}$ for which the group velocity is nearly parallel to the wave normal direction. The examples of raypaths for these two frequency ranges are shown in Figures 3g and 3i. Finally, waves in the whole O^+ band propagate along the field line with an example shown in Figure 3k. It should be noted that for all frequency bands, wave refraction due to the magnetic field gradient and curvature leads to more oblique wave normal direction when waves propagate to higher latitude, unless a strong negative radial plasma density gradient produces wave refraction acting against the refraction caused by the magnetic field [e.g., *Chen et al.*, 2009]. It should be noted that magnetic field gradients could also facilitate energy transfer between wave modes through mode conversion at the crossover frequencies, which is not addressed by our analysis; however, this effect is more likely to be important when the maximum gain occurs for waves launched with frequency close to the crossover frequencies.

Figures 3d, 3f, 3h, 3j, and 3l show path-integrated wave gain as a function of latitude for the selected wave frequencies in the five different frequency ranges, with propagation time indicated (in seconds) in the parentheses next to the right vertical axis. For the case in Figure 3d with $f = 0.6 f_{H+}$ ($f_{cr1} < f < f_{H+}$), the wave does not grow in amplitude because the frequency of interest exceeds the maximum unstable frequency limited by the value of ring current H^+ anisotropy A_{H+} , $f_{max} = f_{H+} A_{H+} / (A_{H+} + 1)$ [Kennel and Petschek, 1966] with here $A_{H+} = 1.07$ and thus $f_{max} = 0.52 f_{H+}$. Namely, instability at frequency f requires $A_{H+} > (f/f_{H+}) / (f/f_{H+} - 1)$, meaning that higher unstable frequency f requires higher anisotropy A_{H+} . The ray with $f = 0.45 f_{H+}$ (Figure 3f) can grow by several decibels within 2° of the equator and then is subject to damping because this ray becomes oblique rapidly due to unguided nature of ray propagation (Figure 3e). For the guided mode of the He^+ band (Figure 3h), this ray obtains wave gain up to 30 dB at $\lambda = 5^\circ$, in part because the presence of heavy He^+ reduces the proton resonant energy and thus increases the growth rate and also because this ray maintains quasi-parallel propagation within 5° of the equator. For the low-frequency portion of the He^+ band (Figure 3j), no growth occurs due to a lack of high-energy protons required for resonance. The same is true for even lower frequency O^+ band (Figure 3l).

Figure 3b summarizes the frequency dependence of maximum wave gain, which is the maximum value of the path-integrated gain along a raypath. The wave gain profile shows two peaks, with the strongest amplification in the He^+ band at frequency close to f_{He+} and the other moderate peak wave gain in the low-frequency portion of the H^+ band. No wave gain is found in the O^+ band. It should be noted that, as *Chen et al.* [2009] have shown, the wave frequency in He^+ band of peak path-integrated wave gain decreases as ion temperature increases, or ion anisotropy decreases, or He^+ ion composition increases or f_{pe}/f_{ce} increases. Given a minor O^+ composition (3%) in our study, the peak frequency in He^+ band more likely stays above the equatorial cross-over frequency.

Knowing the frequency profile of maximum wave gain, we define the maximum wave path-integrated gain in the H^+ , He^+ , and O^+ bands, which can be used to represent and differentiate the amplification levels for each band, as the maximum of wave gain over frequency ranges (f_{cut1}, f_{H+}) , (f_{cut2}, f_{He+}) , and $(0, f_{O+})$, respectively. We repeat the ray tracing results for different locations (L , MLT), at the selected four times. Figure 4 shows the spatial distribution and time evolution of the maximum wave gain in each of the three bands (the top three rows) and the maximum wave gain over all the three bands (the bottom row). Comparison of the maximum wave gain among the three bands shows that the most significant wave gain occurs in the He^+ band in the afternoon sector, associated with the high-density plasmaspheric drainage plume. The plume region is indicated by the magenta contours of $f_{pe}/f_{ce} = 10$, instead of the 50 cm^{-3} contours of cold plasma density (Figure 2), which are a good indicator for the location of the plasmopause. Little wave gain (< 2 dB) is obtained in the O^+ band. The H^+ band can occasionally be stronger than the He^+ band in the inner L shell (~ 3) in the premidnight sector, due to the development of high ring current anisotropy (~ 2 , shown in Figure 2). Now we look at the temporal evolution of the maximum wave gain over all the three bands in the bottom row of Figure 4. At the prestorm (t_1), simulation shows little EMIC wave activity, primarily because the injected ring current ions have not yet been transported toward the high-density plasmasphere, and strong anisotropies have not been developed in the region indicating the plume (by the magenta contour in the bottom right panel of Figure 4). During the main phase (t_2) until the Dst minimum (t_3), the EMIC wave

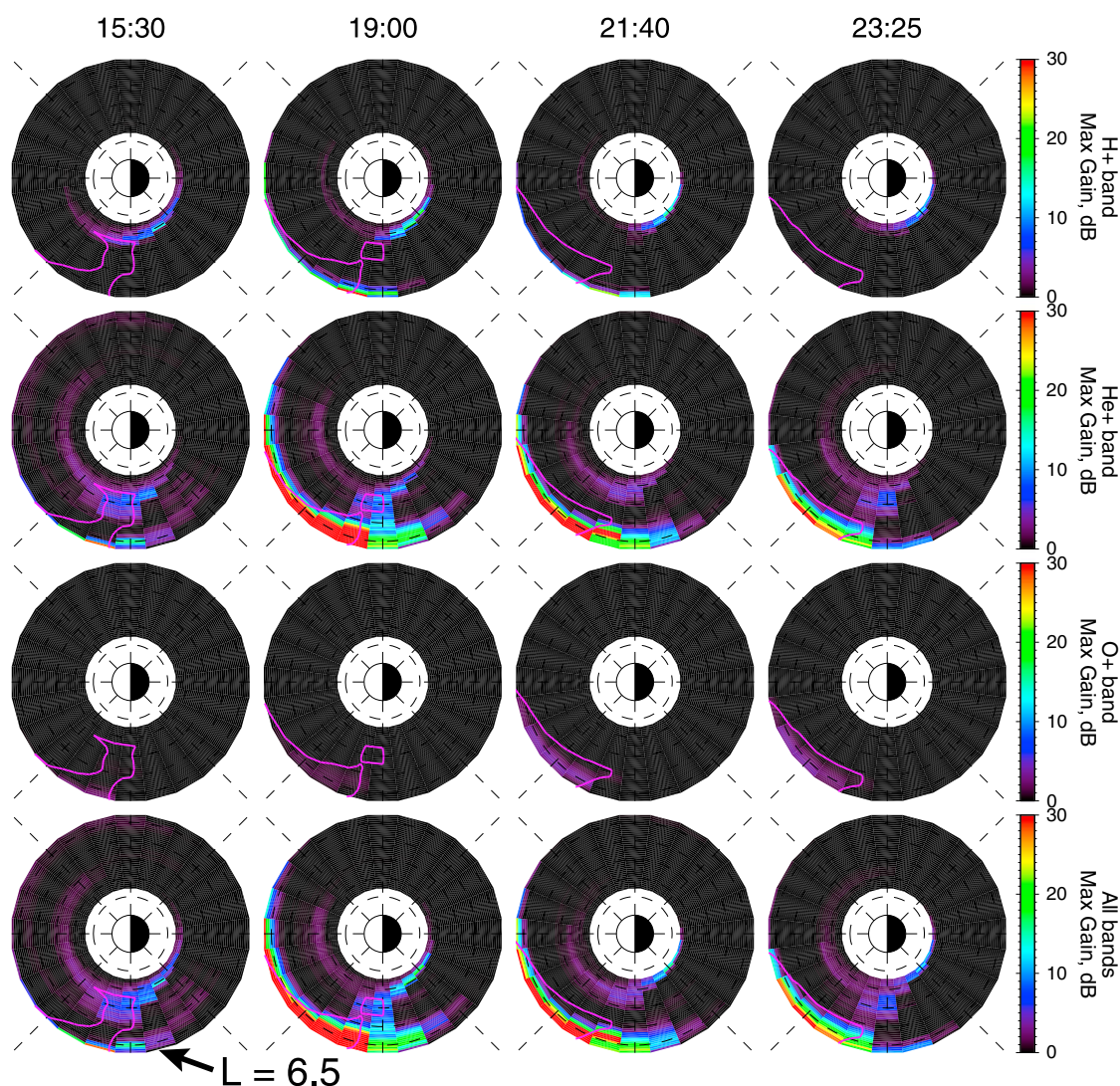


Figure 4. Simulation results of the maximum wave path-integrated gain, from top to bottom, over the H+ band, the He+ band, and the O+ band and all the bands, as a function of ray launch locations (equatorial plane) at the selected times on 9 June 2001. Magenta lines delineate the contours of $f_{pe}/f_{ce} = 10$ as a proxy for the location of the plasmaspheric plume.

gain increases significantly, especially in the plasmaspheric plume. This time interval has a preferential condition for EMIC wave excitation, i.e., the development of anisotropic ring current H⁺ ions in the region of the high-density plasmaspheric plume. During the recovery phase (t_4), the ring current anisotropy in the plume region decreases, leading to smaller wave gains and narrower spatial regions of wave gain exceeding 20 dB.

4. Data Model Comparison

Next we compare the wave simulation with EMIC wave observation or EMIC wave proxy based on observations from five satellites at the geosynchronous orbit, 1994-084, 1991-080, LANL-01A, GOES-8, and GOES-10. The first three satellites do not carry an instrument that directly measures the magnetic field but have magnetospheric plasma analyzers for measuring ring current ions, based on which a proxy of EMIC wave events can be produced using linear kinetic theory. The ring current ion temperature and anisotropy measurement, together with observed cold plasma density, is used to evaluate a wave generation proxy reflecting the linear instability [Blum *et al.*, 2009]. The proxy is later extended to predict wave amplitude based on quantitative comparison between particle observation-based wave proxy and the observed wave amplitude [Blum *et al.*, 2009]. Using this proxy method, EMIC wave events with amplitude estimated to be > 0.1 nT are identified and shown as dots along the satellite trajectories of UT and MLT in Figure 5. For the two GOES satellites,

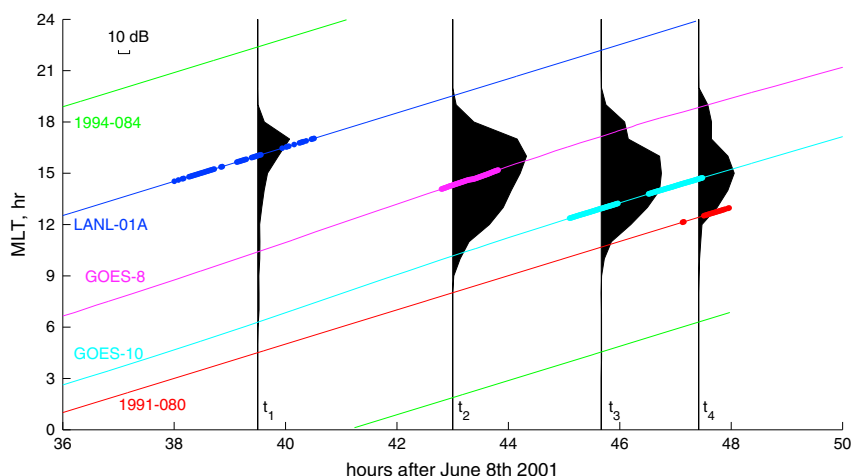


Figure 5. Comparison between EMIC wave observations and simulated maximum wave gain along trajectories of geosynchronous orbiting satellites as a function of UT and MLT. The dot points along the trajectories denote either observation or proxy of EMIC wave event. Four shaded areas represent the MLT distribution of maximum wave path-integrated over all the frequency bands at the selected UTs, with scale of 10 dB shown in the upper left corner.

magnetometers provide direct EMIC wave measurements. EMIC wave events are detected using the automated technique developed by Clausen *et al.* [2011] and are also shown as dots in Figure 5. To compare with the EMIC wave events observed or estimated by proxy, the simulation results of the maximum wave gain over all the bands (the bottom row of Figure 4) at $L = 6.5$ are plotted against MLT at the four selected simulation times, as the shaded areas in Figure 5. The observations and modeling show consistency in that (1) our simulation reproduces the magnetic local time range (12–18 h) where EMIC waves were observed and (2) our simulation also reproduces at which of the five satellites the EMIC wave events are observed and at which are not for the selected four simulation times. It should be emphasized that the four shaded wave gain profiles as a function of MLT correspond to the four different simulation times (t_1 , t_2 , t_3 , and t_4). EMIC waves indirectly inferred from ion data from LANL-01a satellite have longest duration near 15:30 UT before the geomagnetic storm, and the duration and location of waves predicted by LANL-01a is also supported

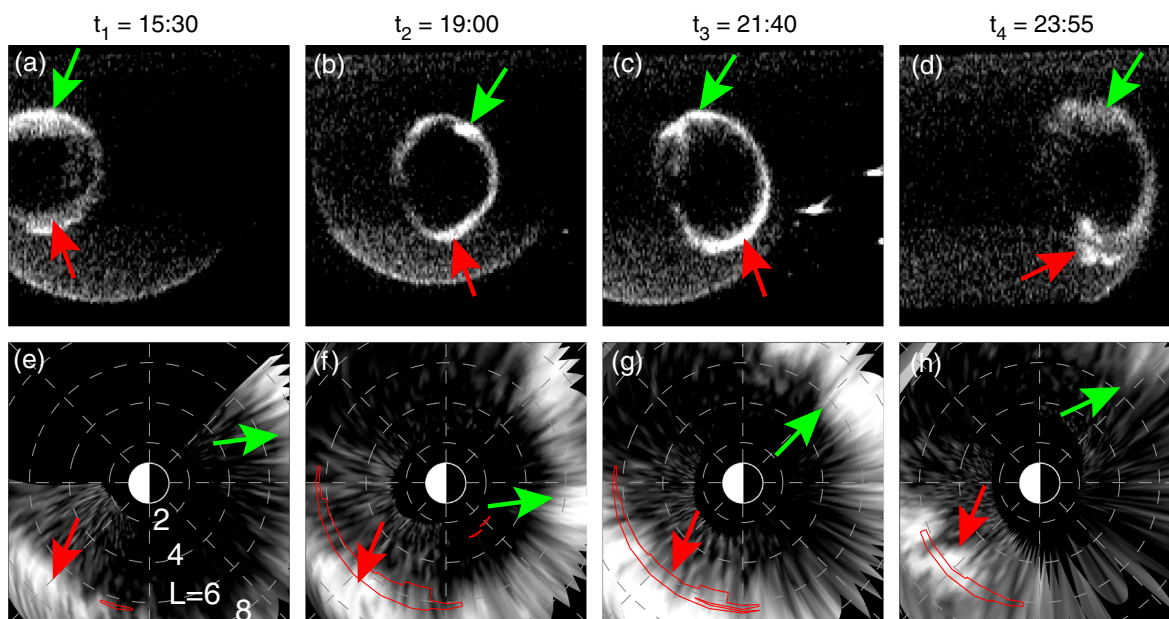


Figure 6. (a–d) Raw proton auroral images from IMAGE FUV SI12 channel at the four selected times on 9 June 2001. (e–h) Comparison between the proton auroral images projected on the SM equatorial plane using T04s magnetic field model and the spatial regions of EMIC wave maximum path-integrated gain exceeding 20 dB (enclosed by red lines).

by the IMAGE FUV observation (shown later in Figure 6e). Our simulation of wave gain however only predicts weaker wave gain over a narrow range of MLTs, while the larger wave gain is predicted near t_2 and t_3 where the wave duration observed by GOES satellites seems shorter than t_1 . This inconsistency at t_1 is probably due to the fact that there was a slight dip in Dst early in the day of the 9th, which might be responsible for wave activities just before the onset of the geomagnetic storm. We also compare the wave amplitude between t_1 and t_2 (not shown). The wave amplitude near t_1 inferred from LANL-01a observation is mostly below 1 nT with the median amplitude of ~ 0.5 nT, which is weaker than the wave amplitude ($\sim 1\text{--}3$ nT) at t_2 and t_3 directly observed by GOES satellites. The wave amplitude comparison tends to agree with the wave gain comparison, but one should be careful in comparing GOES observations to LANL proxy estimates for wave amplitude in too much detail because of different dataset and different methods for obtaining wave amplitude.

In order to compare with EMIC wave simulation in a global context, we take advantage of the far ultraviolet (FUV) Spectrographic Imager (SI) [Mende et al., 2000] onboard the IMAGE satellite [Burch, 2000], specifically the SI12 channel which produces global image of the proton aurora by detecting Doppler-shifted Lyman- α emission (121.8 nm) from precipitating protons. EMIC waves can produce effective pitch angle scattering of ring current ions and lead to precipitation of the protons into the lower atmosphere. Therefore, the observed proton aurora might indicate the EMIC wave events when other precipitation mechanisms are not in effect [e.g., Spasojević et al., 2004; Jordanova et al., 2007]. Raw images of the proton aurora with resolutions of 128×128 pixels taken at the times closer to the four selected simulation times are shown Figures 6a–6d, which are projected on the solar magnetic (SM) equatorial plane using the T04s magnetospheric field model [Tsyganenko et al., 2003; Tsyganenko and Sitnov, 2005] in Figures 6e–6h. We use Tsyganenko model instead of simulated magnetic field line (SCB) for mapping, due to the following two reasons. Firstly, replacing the Tsyganenko model implemented within the IMAGE/FUV software with SCB model is not a trivial task and is beyond the scope of this paper. Secondly SCB model uses the same Tsyganenko model for outer boundary at $L = 6.5$ and the difference between the two models should be small if any because the geomagnetic storm under investigation is not a particularly large storm (Dst -40 nT). The projection of proton aurora is shown in the bottom row of Figure 6. Local noon is roughly toward the bottom left corners of the raw images and toward the left of the projected images. For the raw images, the diffusive patches appearing below main bulk of proton aurora is due to dayglow in the sunlit conditions, which results in the slight enhancement in the instrument counts. These patches appear as gray patches at lower L near noon in the projected images and are not related to real proton precipitation. To make comparison with EMIC wave simulation, the 20 dB contours of the maximum wave gain over all the bands shown in the bottom panel of Figure 4 are superimposed by red lines on the projected images. At t_1 , the bulk area of brightness well describes the main proton aurora (indicated by the green arrows), generally confined to $L > 6$ and extending from premidnight to post-midnight, predominately due to current sheet scattering [Gvozdevskij and Sergeev, 1995] and little due to precipitation by EMIC waves. The precipitation in the afternoon (indicated by the red arrows), from $\sim 14\text{--}17$ MLT and $L > 6$, appears to be consistent with EMIC waves driven precipitation. This is the same region where LANL-01A has the positive proxy (Figure 5). This is also consistent with our simulation where EMIC waves with wave gain > 20 dB (enclosed by the red lines) occurs only near 17 MLT just along the east edge of the plume (bottom left panel of Figure 4). However, the majority of proton aurora observed on the afternoon sector is beyond our simulation domain ($L \leq 6.5$). During the storm time (t_2 and t_3), the proton aurora extends earthward to $L \sim 5$ in the local time range from noon to dusk, which agrees with the region of wave gain > 20 dB (enclosed by the red lines). Finally at t_4 , although the main proton aurora becomes faint due to reduction of plasma sheet ion injection, the afternoon aurora are still intense in a narrower local time range compared with t_2 and t_3 . The reduction in the local time range of proton aurora in the afternoon sector is consistent with the reduction of the local time of EMIC wave gain exceeding 20 dB, although the red contour of wave gain > 20 dB does not match exactly the area of the strong proton aurora, particularly at lower L (~ 5) or at earlier magnetic local time (~ 13 h). Nonetheless, a moderate wave gain (~ 10 dB) is predicted at those regions. Besides t_1 , there is also correspondence at the other three times between EMIC waves at the geosynchronous orbit and the proton precipitation (Figures 5 and 6), specifically the wave observation from GOES-8 at t_2 , the wave observation from GOES-10 at t_3 and t_4 , and the wave proxy from 1991-080 at t_4 .

5. Conclusions and Discussion

The temporal evolution and the spatial distribution of EMIC waves at all the three bands in the inner magnetosphere ($L < 6.5$) have been modeled using a combination of RAM-SCB and HOTRAY codes for the 8–11 June 2001 geomagnetic storm selected as one of the GEM/PMI challenge events. The simulation results are then compared with in situ EMIC wave events and EMIC wave event proxies derived from the geosynchronous satellite observation and also with proton aurora images obtained from the IMAGE satellite. The principal conclusions of this study are summarized as follows:

1. Simulation shows that the strongest EMIC wave amplification in the inner magnetosphere occurs in the He^+ band at large L (>5) in the afternoon where high-density plasmaspheric drainage plume overlaps with enhanced ring current proton anisotropy. Much weaker EMIC wave excitation, dominated in the H^+ band, occurs at lower L inside the plasmasphere in the premidnight sector.
2. Simulation shows that EMIC wave gain occurs in the spatially limited region before the geomagnetic storm, reaching the maximum during the main phase over a broader spatially region at $L > 5$ and over MLT range from noon to dusk. Into the recovery phase, the EMIC wave gain decreases and the region of EMIC wave excitation is reduced.
3. The temporal evolution and local time distribution of simulated EMIC waves are qualitatively consistent with observations at geosynchronous satellites, including EMIC wave events from GOES-8 and GOES-10 and EMIC wave proxy derived from ion measurement of the three LANL satellites.
4. The spatial distribution of simulated EMIC waves is also consistent with the equatorial portion of the proton aurora from the IMAGE satellite, suggesting that such ion precipitation is produced by pitch angle scattering due to the EMIC waves. There is also correspondence between in situ EMIC waves or their proxy at the geosynchronous orbit and the proton precipitation.

In conclusion, the coupled RAM-SCB and HOTRAY model reproduced reasonably well the excitation of EMIC waves and their temporal and spatial evolution during the 8–11 June 2001 storm. Three future improvements could make the model more physical and self-consistent. These include an extension of our model to include the effect of wave-particle interaction feedbacks. EMIC waves, after being generated from ring current ion anisotropic instability, will produce energy and pitch angle scattering on ring current ion population. The change in the ion velocity distribution (energy and pitch angle) leads to the change of ion kinetic motions and thus can affect the spatial distribution of ions too. The pitch angle scattering into the atmospheric loss cone due to the wave-particle interaction will provide additional loss of ring current ions. The wave-induced ion loss would be greatly enhanced during main phase of magnetic storm when the most intense waves are present, and therefore reduce the free energy for EMIC waves, in particular, at the earlier local times after western drifting ions are scattered by duskside waves. This would also lead to a more asymmetric ring current than that due to charge-exchange loss alone. The wave-particle interaction feedback can be treated as a diffusion in both pitch angle and energy [e.g., *Jordanova et al.*, 1998]. To include this, we will need in the modeling the frequency spectrum of EMIC waves, which can be obtained from our wave model, and an algorithm to obtain wave amplitude from the linear wave gain. An improvement of previous studies using semiempirical wave models [e.g., *Jordanova et al.*, 2001] becomes possible recently with the correlation study between the linear growth and the saturated amplitude using *Bortnik et al.* [2011]. Due to this positive correlation, the modeled path-integrated gain distribution indeed reflects the saturated wave amplitude.

Future improvement will also include ray tracing in a self-consistent magnetic field. A dipole magnetic field model is currently implemented in the HOTRAY code. However, the current created by the plasma pressure gradient of ring current ions will perturb the dipole field, leading to compression and stretching of magnetic field at the inner magnetosphere. Compression of magnetic field lines can lead to enhanced path-integrated gain of EMIC waves by keeping the wave normal angle less oblique than otherwise. A more stretched field line tends to enhance wave refraction, and therefore results in less path-integrated gain. For this moderate storm (-40 nT Dst), the distortion in the magnetic field is not significant in the inner duskside magnetosphere, where largest wave-gain is produced, and thus will not affect our results significantly. However, the effect of magnetic field distortions on the EMIC wave gain might not be neglected for a strong geomagnetic storm.

Due to the fact that the RAM-SCM model currently relies on the use of geosynchronous ion flux as the outer boundary, the simulation can not capture the EMIC waves beyond $L > 6.5$ and thus can not reproduce the proton precipitation observed by IMAGE at larger L on the afternoon sector. The third improvement will extend the outer boundary to larger L . This can be accomplished by coupling with other global models, such as the Rice Convection Model [Toffoletto *et al.*, 2003, and references therein] and global magnetohydrodynamics model. Those models will provide boundary fluxes for the RAM-SCB model where more dedicated kinetic treatment takes place.

Appendix A: Characteristic Frequencies Below the Proton Gyrofrequency

A variety of characteristic frequencies appear below the proton gyrofrequency Ω_{H^+} in the cold dispersion relation of multi-ion ($H^+ - He^+ - O^+$) plasma. An example of the dispersion solution is plotted in Figure 3a with ion concentration $\eta_{H^+} = 77\%$, $\eta_{He^+} = 20\%$ and $\eta_{O^+} = 3\%$. The characteristic frequencies, in addition to heavier ion gyrofrequencies (Ω_{He^+} and Ω_{O^+}), include two crossover frequencies (ω_{cr1} and ω_{cr2}), two bi-ion frequencies (ω_{bi1} and ω_{bi2}), and two cutoff frequencies (ω_{cut1} and ω_{cut2}), where subscripts $_1$ and $_2$ denote in the frequency range $[\Omega_{He^+}, \Omega_{H^+})$ and $[\Omega_{O^+}, \Omega_{He^+})$, respectively. The expressions of these frequencies are given below, where two reasonable approximations in the inner magnetosphere, $\omega \ll |\Omega_e|$ and $\omega_{pe}^2 / (\omega |\Omega_e|) \gg 1$, are implicitly utilized.

The two crossover frequencies ω_{cr1} and ω_{cr2} are solutions of $R - L = 0$, where R and L are the Stix coefficients [Stix, 1992]. It follows that the crossover frequencies are the roots of the following equation:

$$A_1 \omega^4 + B_1 \omega^2 + C_1 = 0, \quad (A1)$$

where $A_1 = 1 + x + y$, $B_1 = -[\Omega_{He^+}^2 + \Omega_{O^+}^2 + x(\Omega_{H^+}^2 + \Omega_{O^+}^2) + y(\Omega_{H^+}^2 + \Omega_{He^+}^2)]$, and $C_1 = \Omega_{He^+}^2 \Omega_{O^+}^2 + x \Omega_{H^+}^2 \Omega_{O^+}^2 + y \Omega_{H^+}^2 \Omega_{He^+}^2$. Here $x = \eta_{He^+} / \eta_{H^+}$ and $y = \eta_{O^+} / \eta_{H^+}$. Therefore,

$$\omega_{cr1} = \sqrt{\frac{-B_1 + \sqrt{B_1^2 - 4A_1 C_1}}{2A_1}} \quad (A2)$$

and

$$\omega_{cr2} = \sqrt{\frac{-B_1 - \sqrt{B_1^2 - 4A_1 C_1}}{2A_1}}. \quad (A3)$$

The two cutoff frequencies ω_{cut1} and ω_{cut2} are solutions of $L = 0$, which can be reduced to the following quadratic equation:

$$A_2 \omega^2 + B_2 \omega + C_2 = 0 \quad (A4)$$

where $A_2 = 1 + x + y$, $B_2 = -[\Omega_{He^+} + \Omega_{O^+} + x(\Omega_{H^+} + \Omega_{O^+}) + y(\Omega_{H^+} + \Omega_{He^+})]$, $C_2 = \Omega_{He^+} \Omega_{O^+} + x \Omega_{H^+} \Omega_{O^+} + y \Omega_{H^+} \Omega_{He^+}$. Therefore,

$$\omega_{cut1} = \frac{-B_2 + \sqrt{B_2^2 - 4A_2 C_2}}{2A_2} \quad (A5)$$

and

$$\omega_{cut2} = \frac{-B_2 - \sqrt{B_2^2 - 4A_2 C_2}}{2A_2}. \quad (A6)$$

The two bi-ion resonant frequencies ω_{bi1} and ω_{bi2} are the roots of $R + L = 0$, which can also be reduced to the following equation:

$$A_3 \omega^4 + B_3 \omega^2 + C_3 = 0 \quad (A7)$$

where $A_3 = \Omega_{H^+} + x\Omega_{He^+} + y\Omega_{O^+}$, $B_3 = -[\Omega_{H^+}(\Omega_{He^+}^2 + \Omega_{O^+}^2) + x\Omega_{He^+}(\Omega_{H^+}^2 + \Omega_{O^+}^2) + y\Omega_{O^+}(\Omega_{H^+}^2 + \Omega_{He^+}^2)]$, and $C_3 = \Omega_{H^+}\Omega_{He^+}^2\Omega_{O^+}^2 + x\Omega_{He^+}\Omega_{H^+}^2\Omega_{O^+}^2 + y\Omega_{O^+}\Omega_{H^+}^2\Omega_{He^+}^2$.

Thus,

$$\omega_{bi1} = \sqrt{\frac{-B_3 + \sqrt{B_3^2 - 4A_3C_3}}{2A_3}} \quad (A8)$$

and

$$\omega_{bi2} = \sqrt{\frac{-B_3 - \sqrt{B_3^2 - 4A_3C_3}}{2A_3}}. \quad (A9)$$

Acknowledgments

The authors would like to acknowledge NASA grants NNX13AI61G and NNX11AR64G. Work at Los Alamos was conducted under the auspices of the United States Department of Energy with partial support from NASA/LWS and NSF/GEM program. Work at Stanford was supported by NSF award 0902846. Interplanetary data were provided by the CDAWeb at NASA, and the *Dst* indices were provided by the World Data Center in Kyoto, Japan.

Robert Lysak thanks Jay Johnson and Andrei Demekhov for their assistance in evaluating this paper.

References

- Blum, L. W., E. A. MacDonald, S. P. Gary, M. F. Thomsen, and H. E. Spence (2009), Ion observations from geosynchronous orbit as a proxy for ion cyclotron wave growth during storm times, *J. Geophys. Res.*, **114**, A10214, doi:10.1029/2009JA014396.
- Blum, L. W., E. A. MacDonald, L. B. N. Clausen, and X. Li (2012), A comparison of magnetic field measurements and a plasma-based proxy to infer EMIC wave distributions at geosynchronous orbit, *J. Geophys. Res.*, **117**, A05220, doi:10.1029/2011JA017474.
- Bortnik, J., N. Omid, L. Chen, R. M. Thorne, and R. B. Horne (2011), Saturation characteristics of electromagnetic ion cyclotron waves, *J. Geophys. Res.*, **116**, A09219, doi:10.1029/2011JA016638.
- Burch, J. L. (2000), IMAGE mission overview, *Space Sci. Rev.*, **91**, 1–14.
- Chen, L., R. M. Thorne, and R. B. Horne (2009), Simulation of EMIC wave excitation in a model magnetosphere including structured high-density plumes, *J. Geophys. Res.*, **114**, A07221, doi:10.1029/2009JA014204.
- Chen, L., R. M. Thorne, V. K. Jordanova, C. Wang, M. Gkioulidou, L. Lyons, and R. B. Horne (2010), Global simulation of EMIC wave excitation during the 21 April 2001 storm from coupled RCM-RAM-HOTRAY modeling, *J. Geophys. Res.*, **115**, A07209, doi:10.1029/2009JA015075.
- Chen, L., R. M. Thorne, and J. Bortnik (2011), The controlling effect of ion temperature on EMIC wave excitation and scattering, *Geophys. Res. Lett.*, **38**, L16109, doi:10.1029/2011GL048653.
- Clausen, L. B. N., J. B. H. Baker, J. M. Ruohoniemi, and H. J. Singer (2011), EMIC waves observed at geosynchronous orbit during solar minimum: Statistics and excitation, *J. Geophys. Res.*, **116**, A10205, doi:10.1029/2011JA016823.
- Cornwall, J. M., F. V. Coroniti, and R. M. Thorne (1970), Turbulent loss of ring current protons, *J. Geophys. Res.*, **75**, 4699, doi:10.1029/JA075i025p04699.
- Cornwall, J. M., F. V. Coroniti, and R. M. Thorne (1971), Unified theory of SAR arc formation at the plasmopause, *J. Geophys. Res.*, **76**, 4428, doi:10.1029/JA076i019p04428.
- Erlanson, R., and A. Ukhorskiy (2001), Observations of electromagnetic ion cyclotron waves during geomagnetic storms: Wave occurrence and pitch angle scattering, *J. Geophys. Res.*, **106**(A3), 3883–3895.
- Fraser, B. J., R. S. Grew, S. K. Morley, J. C. Green, H. J. Singer, T. M. Loto'aniu, and M. F. Thomsen (2010), Storm time observations of electromagnetic ion cyclotron waves at geosynchronous orbit: GOES results, *J. Geophys. Res.*, **115**, A05208, doi:10.1029/2009JA014516.
- Gary, S. P., K. Liu, and L. Chen (2012), Alfvén-cyclotron instability with singly ionized helium: Linear theory, *J. Geophys. Res.*, **117**, A08201, doi:10.1029/2012JA017740.
- Gomberoff, L., and R. Neira (1983), Convective growth rate of ion cyclotron waves in a $H^+ - He^+$ and $H^+ - He^+ - O^+$ plasma, *J. Geophys. Res.*, **88**, 2170–2174.
- Gvozdevskij, B. B., and V. A. Sergeev (1995), Scattering on a current sheet—A possible mechanism of auroral proton precipitation, *Geomag. Aeron.*, **35**, 151–155.
- Horne, R. B. (1989), Path-integrated growth of electrostatic waves: The generation of terrestrial myriametric radiation, *J. Geophys. Res.*, **94**(A7), 8895–8909.
- Horne, R. B., and R. Thorne (1993), On the preferred source location for the convective amplification of ion cyclotron waves, *J. Geophys. Res.*, **98**(A6), 9233–9247.
- Horne, R. B., and R. Thorne (1994), Convective instabilities of electromagnetic ion cyclotron waves in the outer magnetosphere, *J. Geophys. Res.*, **99**(A9), 17,259–17,273.
- Horne, R. B., and R. Thorne (1997), Wave heating of He^+ by electromagnetic ion cyclotron waves in the magnetosphere: Heating near the $H^+ - He^+$ bi-ion resonance frequency, *J. Geophys. Res.*, **102**(A6), 11,457–11,471.
- Hu, Y., R. E. Denton, and J. R. Johnson (2010), Two-dimensional hybrid code simulation of electromagnetic ion cyclotron waves of multi-ion plasmas in a dipole magnetic field, *J. Geophys. Res.*, **115**, A09218, doi:10.1029/2009JA015158.
- Johnson, J. R., and C. Z. Cheng (1999), Can Ion Cyclotron Waves Propagate to the Ground?, *Geophys. Res. Lett.*, **26**, 671–674, doi:10.1029/1999GL900074.
- Jordanova, V. K., L. M. Kistler, J. U. Kozyra, G. V. Khazanov, and A. F. Nagy (1996), Collisional losses of ring current ions, *J. Geophys. Res.*, **101**, 111–126, doi:10.1029/95JA02000.
- Jordanova, V. K., J. U. Kozyra, A. F. Nagy, and G. V. Khazanov (1997), Kinetic model of the ring current-atmosphere interactions, *J. Geophys. Res.*, **102**, 14,279–14,292, doi:10.1029/96JA03699.
- Jordanova, V. K., C. J. Farrugia, J. M. Quinn, R. M. Thorne, K. W. Ogilvie, R. P. Lepping, G. Lu, A. J. Lazarus, M. F. Thomsen, and R. D. Belian (1998), Effect of wave-particle interactions on ring current evolution for January 10–11, 1997: Initial results, *Geophys. Res. Lett.*, **25**, 2971–2974, doi:10.1029/98GL00649.

- Jordanova, V. K., C. J. Farrugia, R. M. Thorne, G. V. Khazanov, G. D. Reeves, and M. F. Thomsen (2001), Modeling ring current proton precipitation by electromagnetic ion cyclotron waves during the May 14–16, 1997, storm, *J. Geophys. Res.*, *106*, 7–22, doi:10.1029/2000JA002008.
- Jordanova, V. K., Y. S. Miyoshi, S. Zaharia, M. F. Thomsen, G. D. Reeves, D. S. Evans, C. G. Mouikis, and J. F. Fennell (2006), Kinetic simulations of ring current evolution during the Geospace Environment Modeling challenge events, *J. Geophys. Res.*, *111*, A11S10, doi:10.1029/2006JA011644.
- Jordanova, V. K., M. Spasojevic, and M. F. Thomsen (2007), Modeling the electromagnetic ion cyclotron wave-induced formation of detached subauroral proton arcs, *J. Geophys. Res.*, *112*, A08209, doi:10.1029/2006JA012215.
- Jordanova, V. K., J. Albert, and Y. Miyoshi (2008), Relativistic electron precipitation by EMIC waves from self-consistent global simulations, *J. Geophys. Res.*, *113*, A00A10, doi:10.1029/2008JA013239.
- Jordanova, V. K., S. Zaharia, and D. T. Welling (2010), Comparative study of ring current development using empirical, dipolar, and self-consistent magnetic field simulations, *J. Geophys. Res.*, *115*, A00J11, doi:10.1029/2010JA015671.
- Jordanova, V. K., D. T. Welling, S. G. Zaharia, L. Chen, and R. M. Thorne (2012), Modeling ring current ion and electron dynamics and plasma instabilities during a high-speed stream driven storm, *J. Geophys. Res.*, *117*, A00L08, doi:10.1029/2011JA017433.
- Kennel, C., and H. Petschek (1966), Limit on stably trapped particle fluxes, *J. Geophys. Res.*, *71*(1), 1–28.
- Kozyra, J. U., T. E. Cravens, A. F. Nagy, E. G. Fontheim, and R. S. B. Ong (1984), Effects of energetic heavy ions on electromagnetic ion cyclotron wave generation in the plasmopause region, *J. Geophys. Res.*, *89*, 2217–2233, doi:10.1029/JA089iA04p02217.
- Lee, D.-H., J. R. Johnson, K. Kim, and K.-S. Kim (2008), Effects of heavy ions on ULF wave resonances near the equatorial region, *J. Geophys. Res.*, *113*, A11212, doi:10.1029/2008JA013088.
- Loto'aniu, T. M., B. J. Fraser, and C. L. Waters (2005), Propagation of electromagnetic ion cyclotron wave energy in the magnetosphere, *J. Geophys. Res.*, *110*, A07214, doi:10.1029/2004JA010816.
- Mende, S. B., et al. (2000), Far ultraviolet imaging from the IMAGE spacecraft. 3. Spectral imaging of Lyman- α and OI 135.6 nm, *Space Sci. Rev.*, *91*, 287–318.
- Miyoshi, Y., K. Sakaguchi, K. Shiokawa, D. Evans, J. Albert, M. Connors, and V. Jordanova (2008), Precipitation of radiation belt electrons by EMIC waves, observed from ground and space, *Geophys. Res. Lett.*, *35*, L23101, doi:10.1029/2008GL035727.
- Omidi, N., J. Bortnik, R. Thorne, and L. Chen (2013), Impact of cold O⁺ ions on the generation and evolution of EMIC waves, *J. Geophys. Res. Space Physics*, *118*, 434–445, doi:10.1029/2012JA018319.
- Rasmussen, C. E., S. M. Guiter, and S. G. Thomas (1993), A two-dimensional model of the plasmasphere—Refilling time constants, *Planet. Space Sci.*, *41*, 35–43, doi:10.1016/0032-0633(93)90015-T.
- Rauch, J. L., and A. Roux (1982), Ray tracing of ULF waves in a multicomponent magnetospheric plasma - Consequences for the generation mechanism of ion cyclotron waves, *J. Geophys. Res.*, *87*, 8191–8198, doi:10.1029/JA087iA10p08191.
- Sakaguchi, K., Y. Miyoshi, E. Spanswick, E. Donovan, I. R. Mann, V. Jordanova, K. Shiokawa, M. Connors, and J. C. Green (2012), Visualization of ion cyclotron wave and particle interactions in the inner magnetosphere via THEMIS-ASI observations, *J. Geophys. Res.*, *117*, A10204, doi:10.1029/2012JA018180.
- Shoji, M., Y. Omura, B. Grison, J. Pickett, I. Dandouras, and M. Engebretson (2011), Electromagnetic ion cyclotron waves in the helium branch induced by multiple electromagnetic ion cyclotron triggered emissions, *Geophys. Res. Lett.*, *38*, L17102, doi:10.1029/2011GL048427.
- Soria-Santacruz, M., M. Spasojevic, and L. Chen (2013), EMIC waves growth and guiding in the presence of cold plasma density irregularities, *Geophys. Res. Lett.*, *40*, 1940–1944, doi:10.1002/grl.50484.
- Spasojević, M., J. Goldstein, D. L. Carpenter, U. S. Inan, B. R. Sandel, M. B. Moldwin, and B. W. Reinisch (2003), Global response of the plasmasphere to a geomagnetic disturbance, *J. Geophys. Res.*, *108*(A9), 1340, doi:10.1029/2003JA009987.
- Spasojević, M., H. U. Frey, M. F. Thomsen, S. A. Fuselier, S. P. Gary, B. R. Sandel, and U. S. Inan (2004), The link between a detached subauroral proton arc and a plasmaspheric plume, *Geophys. Res. Lett.*, *31*, L04803, doi:10.1029/2003GL018389.
- Spasojević, M., L. W. Blum, E. A. MacDonald, S. A. Fuselier, and D. I. Golden (2011), Correspondence between a plasma-based EMIC wave proxy and subauroral proton precipitation, *Geophys. Res. Lett.*, *38*, L23102, doi:10.1029/2011GL049735.
- Stix, T. H. (1992), *Waves in Plasmas*, American Institute of Physics, New York.
- Thorne, R. M., and R. B. Horne (1992), The contribution of ion-cyclotron waves to electron heating and SAR-arc excitation near the storm-time plasmopause, *Geophys. Res. Lett.*, *19*, 417–420, doi:10.1029/92GL00089.
- Thorne, R. M., and R. B. Horne (1994), Energy transfer between energetic ring current H⁺ and O⁺ by electromagnetic ion cyclotron waves, *J. Geophys. Res.*, *99*, 17,275–17,282, doi:10.1029/94JA01007.
- Thorne, R. M., and C. F. Kennel (1971), Relativistic electron precipitation during magnetic storm main phase, *J. Geophys. Res.*, *76*(19), 4446–4453.
- Thorne, R. M., R. B. Horne, V. K. Jordanova, J. Bortnik, and S. Glauert (2006), Interaction of EMIC waves with thermal plasma and radiation belt particles, in *Magnetospheric ULF Waves: Synthesis and New Directions*, *Geophys. Monogr. Ser.*, vol. 169, edited by K. Takahashi et al., pp. 213, AGU, Washington, D. C.
- Toffoletto, F., S. Sazykin, R. Spiro, and R. Wolf (2003), Inner magnetospheric modeling with the Rice Convection Model, *Space Sci. Rev.*, *107*, 175–196, doi:10.1023/A:1025532008047.
- Trakhtengerts, V. Y., and M. J. Rycroft (2008), *Whistler and Alfvén Mode Cyclotron Masers in Space*, Cambridge Univ. Press, Cambridge, U. K.
- Tsyganenko, N. A., and M. I. Sitnov (2005), Modeling the dynamics of the inner magnetosphere during strong geomagnetic storms, *J. Geophys. Res.*, *110*, A03208, doi:10.1029/2004JA010798.
- Tsyganenko, N. A., H. J. Singer, and J. C. Kasper (2003), Storm-time distortion of the inner magnetosphere: How severe can it get?, *J. Geophys. Res.*, *108*(A5), 1209, doi:10.1029/2002JA009808.
- Weimer, D. R. (2001), An improved model of ionospheric electric potentials including substorm perturbations and application to the Geospace Environment Modeling November 24, 1996, event, *J. Geophys. Res.*, *106*, 407–416, doi:10.1029/2000JA000604.
- Xiao, F., L. Chen, Y. He, Z. Su, and H. Zheng (2011), Modeling for precipitation loss of ring current protons by electromagnetic ion cyclotron waves, *J. Atmos. Sol. Terr. Phys.*, *73*, 106–111, doi:10.1016/j.jastp.2010.01.007.
- Yahnin, A., and T. Yahnina (2007), Energetic proton precipitation related to ion cyclotron waves, *J. Atmos. Sol. Terr. Phys.*, *69*, 1690–1706, doi:10.1016/j.jastp.2007.02.010.
- Yahnin, A. G., T. A. Yahnina, H. Frey, and V. Pierrard (2013), Sub-oval proton aurora spots: Mapping relatively to the plasmopause, *J. Atmos. Sol. Terr. Phys.*, *99*, 61–66, doi:10.1016/j.jastp.2012.09.018.
- Young, D. T., S. Perraut, A. Roux, C. de Villedary, R. Gendrin, A. Korth, G. Kremser, and D. Jones (1981), Wave-particle interactions near Ω_{He^+} observed on GEOS 1 and 2. I—Propagation of ion cyclotron waves in He⁺-rich plasma, *J. Geophys. Res.*, *86*, 6755–6772, doi:10.1029/JA086iA08p06755.

- Young, D. T., H. Balsiger, and J. Geiss (1982), Correlations of magnetospheric ion composition with geomagnetic and solar activity, *J. Geophys. Res.*, **87**, 9077–9096, doi:10.1029/JA087iA11p09077.
- Yuan, Z., X. Deng, X. Lin, Y. Pang, M. Zhou, P. M. E. Décréau, J. G. Trotignon, E. Lucek, H. U. Frey, and J. Wang (2010), Link between EMIC waves in a plasmaspheric plume and a detached sub-auroral proton arc with observations of Cluster and IMAGE satellites, *Geophys. Res. Lett.*, **37**, L07108, doi:10.1029/2010GL042711.
- Zaharia, S. (2008), Improved Euler potential method for three-dimensional magnetospheric equilibrium, *J. Geophys. Res.*, **113**, A08221, doi:10.1029/2008JA013325.
- Zaharia, S., C. Cheng, and K. Maezawa (2004), 3-D force-balanced magnetospheric configurations, *Ann. Geophys.*, **22**, 251–265, doi:10.5194/angeo-22-251-2004.
- Zaharia, S., V. K. Jordanova, M. F. Thomsen, and G. D. Reeves (2006), Self-consistent modeling of magnetic fields and plasmas in the inner magnetosphere: Application to a geomagnetic storm, *J. Geophys. Res.*, **111**, A11S14, doi:10.1029/2006JA011619.
- Zaharia, S., V. K. Jordanova, D. Welling, and G. Tóth (2010), Self-consistent inner magnetosphere simulation driven by a global MHD model, *J. Geophys. Res.*, **115**, A12228, doi:10.1029/2010JA015915.